

Evidence of Higher Order Topology in Multilayer WTe₂ from Josephson Coupling through Anisotropic Hinge States

Yong-Bin Choi¹, Yingming Xie², Chui-Zhen Chen^{2,†}, Jin-Ho Park¹, Su-Beom Song³, Jiho Yoon⁴, Bum Joon Kim^{1,5}, Takashi Taniguchi⁶, Kenji Watanabe⁶, Hu-Jong Lee¹, Jong-Hwan Kim³, Kin Chung Fong^{7,*}, Mazhar N. Ali^{4,*}, Kam Tuen Law^{2,*} and Gil-Ho Lee^{1,*}

¹Department of Physics, Pohang University of Science and Technology, Pohang, Republic of Korea

²Department of Physics, Hong Kong University of Science and Technology, Clear Water Bay, Hong Kong, China

³Department of Materials Science and Engineering, Pohang University of Science and Technology, Pohang, Republic of Korea

⁴Max Plank Institute for Microstructure Physics, Halle (Saale), Germany

⁵Center for Artificial Low Dimensional Electronic Systems, Institute for Basic Science (IBS), Pohang, Republic of Korea

⁶Research Center for Functional Materials, National Institute for Materials Science, Tsukuba, Ibaraki, Japan;

⁷Raytheon BBN Technologies, Quantum Information Processing Group, Cambridge, MA, USA

†Current address: Institute for Advanced Study and School of Physical Science and Technology, Soochow University, Suzhou 215006, China

*Correspondence and requests for materials should be addressed to K.C.F (kc.fong@raytheon.com), M.N.A. (maz@berkeley.edu), K.T.L. (phlaw@ust.hk), or G.-H.L. (lghman@postech.ac.kr).

The noncentrosymmetric Td-WTe₂, previously known as a type-II Weyl semimetal, is expected to have higher order topological phases with topologically protected, helical one-dimensional (1D) hinge states when their scarcely separated Weyl points get annihilated. However, the detection of these hinge states is difficult in the presence of the semimetallic behaviour of the bulk. Here, we spatially resolved the hinge states by analysing the magnetic field interference of supercurrent in Nb-WTe₂-Nb proximity Josephson junctions. The Josephson current along the *a*-axis of the WTe₂ crystal, but not along the *b*-axis, showed sharp enhancements at the edges of the junction; the amount of enhanced Josephson current was comparable to the upper limits of a single 1D conduction channel. Our experimental observations provide evidence of the higher order topological phase in WTe₂ and its corresponding anisotropic topological hinge states, in good agreement with theoretical calculations. Our work paves the way for hinge transport studies on topological semimetals in superconducting heterostructures, including their topological superconductivity.

Three-dimensional (3D) Dirac and Weyl semimetals (WSMs) are materials which support massless fermionic quasiparticles¹. WTe₂ represented the first example of a new kind of type-II WSM that hosts emergent quasiparticles of Lorentz-violating Weyl fermions, which were forbidden as a fundamental particle in nature and have therefore long been overlooked in quantum field theory^{2,3}. Unique electronic transport signatures, including the intrinsic anomalous Hall effect⁴⁻⁶, magnetic breakdown and Klein tunnelling effect⁷, Landau level spectrum collapse⁸ and the asymmetric Josephson effect⁹, have been subjected to fundamental and application-based studies. WTe₂ is naturally close to a superconducting phase; it was shown to have low-pressure induced superconductivity while its sister phase, MoTe₂, was shown to be the only intrinsically superconducting WSM at 0.3 K with an extreme pressure-driven critical temperature enhancement^{10,11}. Topological boundary states emerge at the surface of bulk WSMs in the form of Fermi arcs that connect projected Weyl points with different chirality in momentum space. However, the small separation of Weyl points in momentum space² makes Fermi arcs of bulk WTe₂ difficult to resolve by angle-resolved photoemission spectroscopy (ARPES)^{12,13}. In the monolayer limit of WTe₂, a two-dimensional (2D) topological insulating phase was predicted to accompany one-dimensional (1D) quantum spin Hall edge states due to large spin-orbit coupling¹⁴, and experimentally verified by electrical transport^{15,16}, ARPES and

scanning tunnelling microscopy (STM)¹⁷⁻¹⁹.

Recently, it was proposed that bulk MoTe_2 and WTe_2 in Td structures are higher order topological insulators (HOTIs), and that large surface states arising from gapped fourfold Dirac surfaces would be present²⁰. Their signatures were actually observed previously but not understood; large surface states not attributable to the Fermi arcs arising from the Weyl points were seen by ARPES and STM in bulk WTe_2 and MoTe_2 ^{21,22}. In addition, WTe_2 was proposed to have topologically protected conducting helical hinge states²⁰, which would coexist with bulk conduction states and be difficult to resolve by transport measurements. However, these hinge states are difficult to observe in transport experiments due to the large contribution from the bulk states. In this work, we couple a WTe_2 thin film to two superconducting leads formed by Nb and measure the critical superconducting current of this Nb- WTe_2 -Nb Josephson junction as a function of applied magnetic field. By analysing the Fraunhofer pattern resulted from the interference of the superconducting currents, we found evidence of conducting channels localised at the edges of the sample, consistent with the presence of topological hinge states due to the higher order topology of WTe_2 . We further found that the hinge states are highly anisotropic; they are localised on edges parallel to the a -axis of the crystal while the hinge states along the b -axis are delocalised and merge with the bulk states. Our claims of the presence of hinge states are supported by theoretical calculations that explain the observed current density profile and Fraunhofer patterns.

Firstly, we describe the angle-dependent electrical transport in multilayer WTe_2 . High-quality single crystals of WTe_2 used in this report were grown by the flux method^{23,24}. There was no intrinsic chemical doping of WTe_2 crystals as confirmed by analysis of Shubnikov-de Haas oscillation in the bulk crystal or classical Hall measurements of the exfoliated multilayer WTe_2 (Fig. S1). Unlike many other transition metal dichalcogenides, such as MoS_2 , MoSe_2 and MoTe_2 , which have hexagonal planar structures, WTe_2 crystallises in the Td structure (orthorhombic SG# 31 Pmn21), wherein the hexagonal plane is distorted by the formation of tungsten chains running along the a -axis (Fig. 1a). This leads to the WSM bulk state and the 2D topological insulating state in the monolayer limit¹⁴. To investigate the in-plane electrical anisotropy of the crystal, we fabricated a multi-terminal circular WTe_2 device covered with hexagonal boron nitride (Fig. 1b). Angular dependence of the in-plane resistance, $R(\theta)$, within a single device was measured with a four-probe configuration to avoid contact resistance. Here, we chose the pair of voltage probes nearest to the pair of current electrodes, as shown in Fig.

1b, where θ denotes the angle between the direction of the resistance measurement (white line) and the a -axis of the WTe_2 crystal (red line). As expected from the crystalline anisotropy, the minimum resistance was observed along the a -axis ($\theta = 0$) and the maximum resistance was observed along the b -axis ($\theta = 90^\circ$) (Fig. 1c). The ratio of maximum to minimum resistance reached 2.7 at 50 K and dropped to 2.3 at 4.2 K (inset of Fig. 1c). Other manifestations of such anisotropic transport of WTe_2 have been studied in quantum oscillations²⁵ and the chiral anomaly²⁶. As the anisotropic crystallographic axes are also reflected in the symmetry of lattice vibrations, polarisation-resolved Raman spectroscopy^{6,27,28} is used to determine the crystal axis for the following devices in an accurate and non-invasive manner. The A1 Raman mode at around 165 cm^{-1} shows a characteristic two-fold pattern in the parallel polarisation configuration of laser excitation and detection (Fig. 1d). The a -axis (b -axis) of the crystal can be determined unambiguously based on the angle with maximum (minimum) intensity, as reported previously (see Figs. S2 and S3 for more data of Raman spectroscopy).

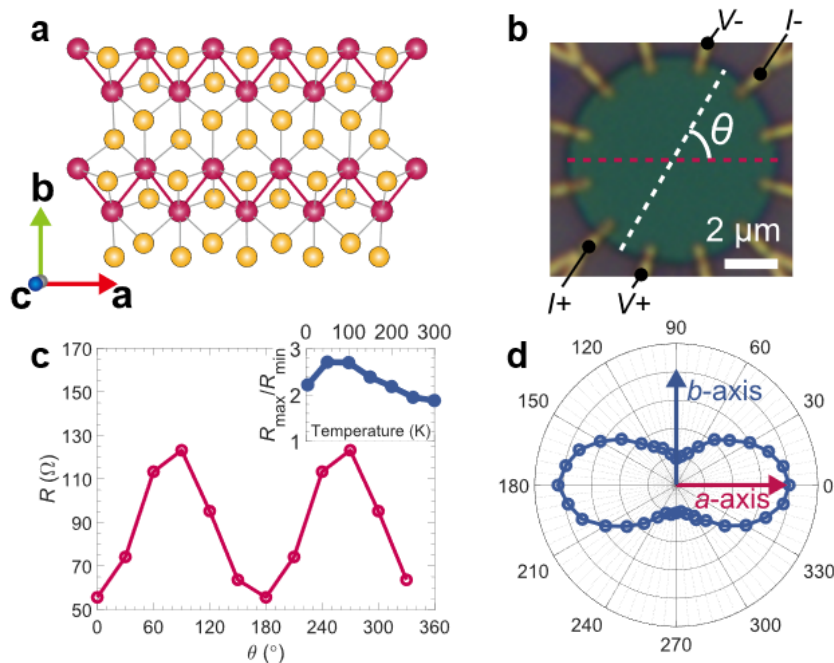


Figure 1 | Anisotropy of WTe_2 crystal. **a**, Schematic of the atomic structure of WTe_2 in the a - b plane. Red (yellow) balls represent the W (Te) atoms. A chain of W atoms forms along the a -axis. **b**, Optical micrograph of a 15-nm thick WTe_2 flake etched into a circular disk shape with multiple gold contact electrodes. θ is the angle between the measurement direction (white line) and the a -axis of the crystal (red line). **c**, Angular dependence of the resistance of the circular

device at 4.2 K. Resistance along the a -axis (b -axis) shows the smallest (largest) value. (Inset) Temperature dependence of the ratio of the maximum to minimum resistance. **d**, Polarisation angle dependence of the A1 phonon mode at $\sim 165 \text{ cm}^{-1}$. The Raman signal shows the maximum (minimum) intensity along the a -axis (b -axis).

Now, we discuss the proximity Josephson junction created with the multilayer WTe₂, where WTe₂ is placed between two Nb superconducting electrodes as depicted in Fig. 2a. When superconducting contacts are electrically transparent, the superconducting order parameters of Nb electrodes can extend into WTe₂ and eventually lead to Josephson coupling, as mediated by WTe₂. We fabricated eight different Josephson junctions of length L between 60 and 230 nm, width W between 1.8 and 5.2 μm and WTe₂ thickness t between 13 and 27 nm. These devices were divided into two groups with different crystal orientations, the a - and b -axes, aligned to the current direction (see Methods for fabrication processes). We will focus on two representative devices, Dev. A of $(L, W, t) = (190 \text{ nm}, 2.3 \mu\text{m}, 13.2 \text{ nm})$ with current flow along the a -axis and Dev. B of $(L, W, t) = (100 \text{ nm}, 3.3 \mu\text{m}, 25.0 \text{ nm})$ with current flow along the b -axis (see Table S1 for a summary of other devices). Figure 2c shows typical current-voltage (I - V) characteristics of Dev. A at various temperatures. While sweeping the bias current from zero to a positive value, the junction voltage switched from zero to a finite value at the Josephson critical current, $I_c = 0.7 \mu\text{A}$. The retrapping current at which the voltage switched from a finite value back to zero was $0.4 \mu\text{A}$, which was smaller than I_c presumably due to self-heating of the junction²⁹. The I_c decreased monotonically with increasing temperature T and eventually vanished around $T = 1.0 \text{ K}$, above which the I - V curve became linear with a slope corresponding to the normal resistance, R_N . As I_c scales with cross-sectional area $A = Wt$, while R_N scales with $1/A$, the $I_c R_N$ product became independent of A such that it characterised the strength of Josephson coupling, taking account of the junction geometry. The measured $I_c R_N$ product of Dev. A (22.4 μV) was about seven times larger than that of Dev. B (3.0 μV). Anisotropy of the $I_c R_N$ product along the a - and b -axes was consistently observed for other six devices. The T -dependence of I_c in Fig. 2d also showed more robust Josephson coupling of Dev. A than Dev. B.

Unlike the insulating bulk states of topological insulators, bulk states of WSMs, like WTe₂, are conducting, making it challenging to resolve the proposed topological hinge states.

Our approach was to spatially resolve how the Josephson current flows through the Nb-WTe₂-Nb Josephson junction by analysing its magnetic field response. When the magnetic field B is threading the junction area, the Aharonov-Bohm effect leads to a macroscopic quantum phase difference between the superconductors and modulates I_c according to the dc Josephson relationship. If a sinusoidal current-phase relation is assumed, the Josephson current interference pattern is determined by the maximum value of the phase-sensitive integration as $I_c(B) = \left| \int_{-\infty}^{\infty} J(x) e^{i\alpha x} dx \right|$, with Josephson current density $J(x)$, where x is the real-space coordinate along the junction width direction, the magnetic field dependent parameter $\alpha = 2\pi B L_{\text{eff}} / \Phi_0$, the effective junction length $L_{\text{eff}} = L + 2L'$ taking into account the magnetic flux penetrating each superconducting electrode by L' , the magnetic flux quantum $\Phi_0 = h/2e$, Plank's constant h , and electron charge e . As $I_c(B)$ can be viewed as the magnitude of the Fourier transform of $J(x)$, we can extract $J(x)$ from the inverse Fourier transform (IFT) of the experimentally measured $I_c(B)$ (Fig. S4) and visualise the current flow density in the junction. This technique has been used for visualising edge-dominant transport of HgTe-based 2D quantum spin Hall insulators (QSHIs)^{30,31} and surface-dominant transport of Bi-based 3D topological insulators³². A related technique with SQUID loop recently provided evidence of hinge states in Bi nanowires³³.

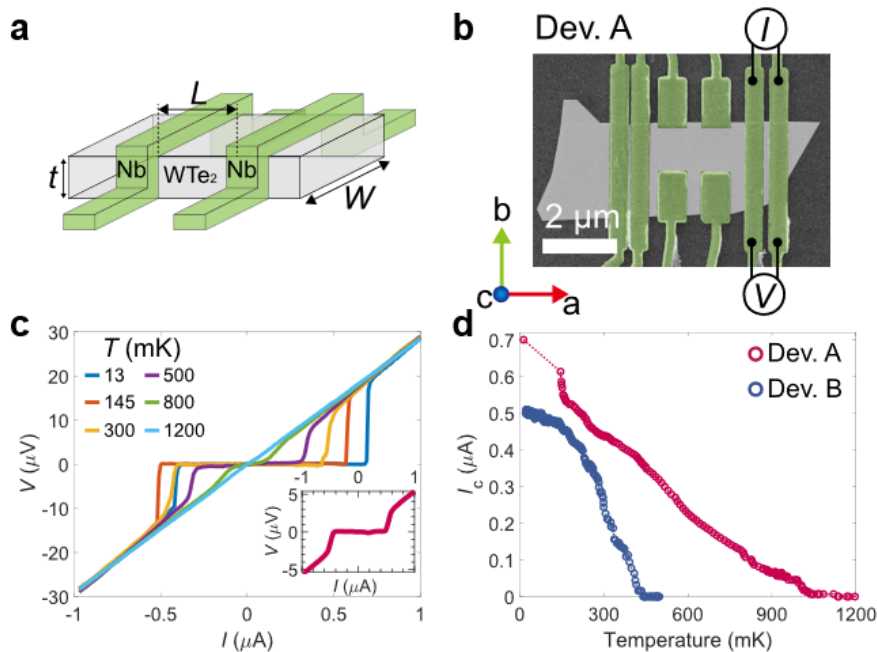


Figure 2 | Characteristics of WTe₂-based Josephson junction. **a**, Schematic of a WTe₂

Josephson junction. W , L , and t represent the junction width, junction length, and thickness of the multilayer WTe₂ flake, respectively. **b**, False-colour scanning electron micrograph of Dev. A showing the measurement configuration. **c**, Typical current-voltage (I - V) characteristics of Dev. A measured by sweeping the bias current from negative to positive at different perpendicular external magnetic field strengths. The lower right inset shows the I - V characteristics of Dev. B without an external magnetic field. **d**, Temperature dependence of the Josephson critical current, I_c , for Dev. A and Dev. B.

Figures 3a and 3d show schematics of Dev. A and Dev. B, respectively, where Nb superconducting electrodes contact the top and both sides of the WTe₂ flake. The topological hinge states are expected to reside on opposite sides of the hinges of the WTe₂ flake (see Fig. S5 for more details). The Fraunhofer pattern of Dev. A is shown in Fig. 3b. The period of the I_c oscillation, $\Delta B = 14.7$ G, corresponded well to the flux quantum threading of an effective junction area of WL_{eff} with $L' \approx 210$ nm, ruling out the possibility of accidental micro-shorts between the Nb electrodes. L' corresponds to the half width of the Nb electrodes, which can be understood by the magnetic flux fully penetrating the Nb electrode. The non-vanishing behaviour of $I_c(B)$ up to $B = 200$ G, shown in Fig. 3b, clearly deviated from the single-slit Fraunhofer pattern (black line in Fig. 3b) expected for a spatially uniform Josephson current density, $J(x) = \text{constant}$. Qualitatively, the non-vanishing behaviour of I_c resembles a SQUID interference pattern for a delta function-like Josephson current density at the junction edges. The $J(x)$ extracted by IFT of $I_c(B)$ for Dev. A (Fig. 3c) clearly showed enhancement of Josephson current density at both edges of the junction, with the baseline arising from the spatially uniform bulk contribution (black dotted line). This was consistent with the expectation of hinge states along the a -axis of the WTe₂ crystal. The width of the Josephson current-carrying hinge states was determined to be around 100 nm using a Gaussian line shape (red dotted line in Fig. 3c). Importantly, we performed a control experiment by fabricating a similar Josephson junction on topologically trivial graphite, to exclude the possibility that the non-vanishing pattern was an artefact (see Fig. S6); as expected, there was no evidence of the non-vanishing pattern. In contrast to Dev. A, Dev. B (Fig. 3d) exhibited an interference pattern resembling the conventional single-slit Fraunhofer pattern, where oscillation amplitude decayed with $1/B$ and vanished above ~ 50 G (Fig. 3e). This was very similar to the results of our control experiment with graphite. The Josephson current density

extracted by IFT showed a uniform current distribution, without any signatures of edge-enhanced transport within the limits of our experimental resolution (Fig. 3f). Six more devices with different crystal axes showed consistent interference patterns and current density distributions (Fig. S7 for a -axis and Fig. S8 for b -axis). The sharp difference in $J(x)$ between Dev. A and Dev. B will be discussed in terms of the distinct shape of the spatial wave functions of topological hinge states along the different crystal axes.

We theoretically investigated the hinge states, and their Fraunhofer patterns, by adopting the model Hamiltonian reported previously^{20,34}, which describes the higher order topological properties of WTe₂ (see Methods for details). Our model showed highly anisotropic band structures (insets of Figs. 3h and 3j), with the helical hinge states showing markedly different localisation along the a - versus b -axis. The wave function of the hinge states along the a -axis was localised at the edges of the junction (Fig. 3h), matching the current density profile of Dev. A (Fig. 3c). When the chemical potential was set to introduce a bulk contribution, the calculated interference pattern in Fig. 3g, taking into account both hinge and bulk states, showed a close resemblance to the interference shape measured in Dev. A (Fig. 3b), especially for the non-vanishing behaviour of I_c even at high B . In contrast, the hinge states along the b -axis were strongly merged into bulk states in momentum space (inset of Fig. 3j). Consequently, the wave function was well delocalised over the whole junction in real space, as plotted in Fig. 3j, which matched the uniform current density profile of Dev. B (Fig. 3f). This resulted in a single-slit Fraunhofer pattern, as shown in Fig. 3i, which was similar to the interference pattern measured for Dev. B (Fig. 3e). The observed Josephson current mediated by a single edge of the junction ($I_{J,\text{side}} = 22$ nA for the left edge and 50 nA for the right edge, visible as the shaded areas in Fig. 3c) was comparable to and, importantly, less than the maximum theoretical value of $I_{J,\text{h}} = 140$ nA for a single hinge state. We arrived at this maximum by considering a short ballistic junction limit ($eI_{J,\text{h}}R_{N,\text{h}} = \pi\Delta_{\text{Nb}}$), where $R_{N,\text{h}} = h/e^2$ is the normal resistance for a single hinge state and $\Delta_{\text{Nb}} = 1.763k_{\text{B}}T_{\text{c,Nb}}$ is the BCS superconducting gap of the Nb electrode with $T_{\text{c,Nb}} = 7.5$ K. $I_{J,\text{side}}$ being smaller than $I_{J,\text{h}}$ was consistent with the theory that there was only one hinge state per side of the WTe₂ flake, as depicted in Figs. 3a and 3d. Similar quantitative issues have been previously discussed in other HOTI candidates^{33,35}.

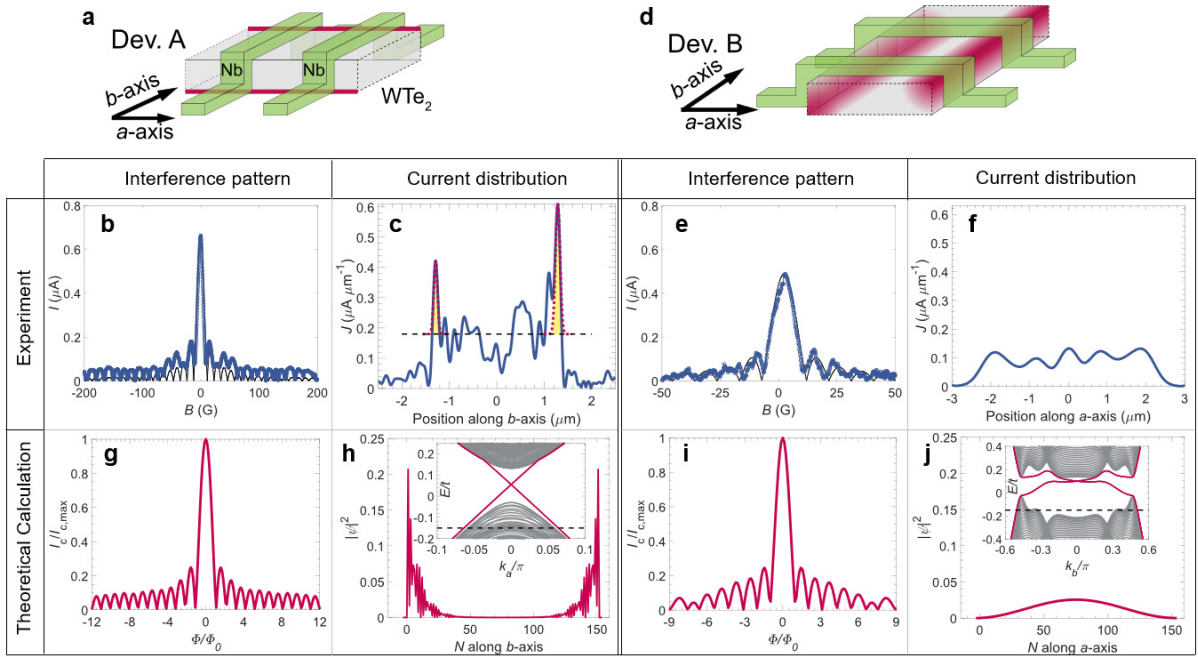


Figure 3 | Interference pattern for the WTe₂ Josephson junction and extracted current profile. **a, d**, Schematics of WTe₂ Josephson junctions with well-localised hinge states along the *a*-axis, represented by thick red lines (**a**, Dev. A), and with delocalised hinge states along the *b*-axis, conceptually represented by blur red lines (**d**, Dev. B) **b, e**, Magnetic field interference patterns of the critical current for Dev. A (**b**) and Dev. B (**e**). Black lines represent a single-slit Fraunhofer pattern of $|\sin(\pi L_{\text{eff}}WB/\Phi_0)/(\pi L_{\text{eff}}WB/\Phi_0)|$. **c, f**, Extracted spatial distribution of the Josephson current density J for Dev. A (**c**) and Dev. B (**f**). Red dotted lines in **c** represent Gaussian fitting for the edge current enhancements on each side of the junction, with the baseline arising from the bulk contribution (black dotted line). **g, i**, Theoretically calculated interference patterns of the critical current along the *a*-axis (**g**) and *b*-axis (**i**). **h, j**, Theoretically calculated wave functions of the hinge states along the *a*-axis (**h**) and *b*-axis (**j**). (Insets) The energy spectra of multilayer WTe₂ along the *a*-axis (**h**) and *b*-axis (**j**). The red lines in the energy spectra represent the helical hinge states and the grey lines represent the bulk states.

We note that there is an alternative, but less likely, explanation for the observation that stems from the QSHI phase of monolayer WTe₂. When monolayers of WTe₂ with 1D quantum spin Hall edge states are vertically stacked with finite interlayer interaction, 1D topological edge states gradually turn into the Fermi arc surface state of WSM. In this few-layer limit

between the bulk and monolayer, there may exist edge states due to quantisation of the c -axis momentum in the Fermi arc states. However, this is unlikely for three reasons. Firstly, we were closer to the bulk limit in our experiments (18 – 38 layers) than the monolayer limit. Secondly, many experiments have been carried out on few-layer (2 – 10 layers) WTe₂, and edge states have been seen strictly in the monolayer¹⁵⁻¹⁹. Finally, the Fermi arcs from the Weyl points in WTe₂ are extremely short and difficult to resolve by ARPES, such that edge states originating from quantisation of Fermi arcs show greater mixing with the bulk states.

By investigating the transport of multilayer WTe₂ in both normal and superconducting regimes in combination with model Hamiltonian calculations, we provided evidence of higher order topology of WTe₂ via proximity-induced superconductivity in anisotropic hinge states. Several theoretical studies on the effect of superconducting proximity on WSMs showed that the Andreev reflection with bulk states is suppressed due to conservation of chirality³⁶, while the topological boundary state interacts well with superconductivity^{37,38}. Such selective coupling of bulk and boundary states to superconductors makes superconducting heterostructures an ideal platform for investigating topological semimetals that have mixed bulk and topological boundary contributions, particularly HOTI systems.

Methods

Device fabrication. WTe₂ single crystal was mechanically exfoliated into WTe₂ thin film of thickness about 10 to 20 nm and placed on Si substrate covered with 300-nm thick insulating SiO₂. Thickness of WTe₂ flakes was confirmed by atomic force microscopy after the electrical measurement. As bulk single crystal has a needle shape elongated along the a -axis, crystal axis could be tracked during the exfoliation process. Polarised Raman spectroscopy was used to confirm the crystal axis direction after the electrical measurement. To eliminate possibly contaminated topmost layers of WTe₂ flake, *in-situ* Argon ion etching was conducted before the metal deposition for removing possibly oxidized WTe₂ surface layers due to ambient air. Ti/Au (5 nm/100 nm) or Ti/Nb/Au (5 nm/100 nm/5 nm) electrode were deposited for studying normal transport or superconducting transport, respectively. Ti layer improves adhesion of metal electrodes to WTe₂, and Au layer protects Nb superconducting electrode from oxidation. The chamber pressure during Ti evaporation was kept lower than 8×10^{-8} Torr. Nb layer in Ar atmosphere was sputtered at slow rate of 8.33 nm/min to minimise the

damage of WTe₂ flake by Ar plasma. In the whole fabrication process, top surface of WTe₂ thin film was exposed Poly-methyl methacrylate (PMMA) polymer only one time to minimise the degradation of WTe₂.

Polarisation-resolved Raman spectroscopy. Raman spectra are obtained with a confocal microscopy set-up at room temperature. The samples are excited with HeNe laser (632.8 nm) at normal incidence. Raman signal is collected in the backscattering configuration and analysed by a monochromator equipped with liquid nitrogen-cooled silicon CCD. Two linear polarisers in the parallel configuration are placed immediately after the laser and before the monochromator to define the polarisations of incident and scattered light, respectively. The crystal orientation relative to the polarisation is controlled with a half waveplate between a beam splitter and WTe₂ flakes.

Effective model. The Td-WTe₂ has been identified as a type-II WSM². However, according to both ab initial calculation¹³ and ARPES measurement¹², its Fermi arc state connecting Weyl points is very short. Observed large arc-like surface states in most previous works are determined to be topologically trivial, and Wang et al.²⁰ recently proposed that large arc-like state are actually the split and gapped Dirac cone surface states in HOTI phase. The HOTI phase in 1T'-WTe₂ or MoTe₂ (monoclinic SG# 11 P2₁/m) has been justified to be driven by the double band inversion at Gamma point^{20,39}. From 1T'-WTe₂ to Td-WTe₂, not only the Weyl points are created, but also the huge arc-like surface states are inherited from original HOTI phase. Considering the small separation between the bulk Weyl points, the HOTI phase in Td-WTe₂ may be readily realised under some realistic conditions, such as the presence of small strain^{20,40}. Since the 1T'- and Td-WTe₂ in HOTI phase exhibit the same topological surface state feature, we would not be able to distinguish them in this work. As we want to probe the topological feature of WTe₂, it is sufficient to use a model Hamiltonian with equivalent topological nature as^{20,34},

$$H(\mathbf{k}) = H_{MN}(\mathbf{k}) + V_c + V_{so}(\mathbf{k}). \quad - \text{Eq. (1)}$$

Here, $H_{MN}(\mathbf{k}) = (m_1 + \sum_{j=a,b,c} v_j \cos(k_j) + m_2 \mu^x + m_3 \mu^z) \tau^z + \lambda_b \sin k_b \mu^y \tau^y + \lambda_c \sin k_c \tau^x$, $V_c = \gamma_x \mu^x + \gamma_z \mu^z$, $V_{so}(\mathbf{k}) = \beta_a \sin k_a \mu^y \tau^y \sigma^z$. The Pauli matrices μ, τ operates on different orbital space, σ operates on spin space. The Hamiltonian $H_{MN}(\mathbf{k})$ gives a bulk monopole node-line (MNL) semimetal²⁰, V_c is a mass term that titles the bulk MNL,

$V_{so}(\mathbf{k})$ gaps the bulk MNL and gives the helical hinge states. The model Hamiltonian $H(\mathbf{k})$ exhibits hinge states and has similar higher order topological properties of WTe₂ or MoTe₂^{20,34}. In the main text Figs. 3g-j, we set $m_1 = -3t$, $m_2 = 0.3t$, $m_3 = 0.2t$, $v_a = 2t$, $v_b = 1.6t$, $v_c = t$, $\lambda_b = 0.1t$, $\lambda_c = t$, $\gamma_x = 0.4t$, $\gamma_z = -0.4t$, $\beta_a = 1.5t$. $t = 1$ is a unit of energy.

Numerical calculation of Josephson current. In the calculation, we assume multilayer WTe₂ underneath Nb electrodes are fully superconducting due to proximity effect and their pairing potentials are set by $\Delta e^{\pm i\phi_0/2}$, respectively. We model multilayer WTe₂ with the lattice model discretising from Hamiltonian $H(\mathbf{k})$ in Eq. (1) and the Josephson current was evaluated by recursive Green's function method⁹ by setting the system with three layers of WTe₂, length to be 25 sites, width to be 150 sites, $k_B T = \Delta/200$, and $\Delta = 0.5$.

Acknowledgements

Y.-B.C. and G.-H.L. were supported by Samsung Science and Technology Foundation under Project Number SSTF-BA1702-05 for device fabrications and low temperature measurements, and National Research Foundation of Korea (NRF) Grant funded by the Korean Government (No. 2016R1A5A1008184). J.K. and S.S. acknowledges the support from the National Research Foundation of Korea grant (No. 2017R1C1B2012729). B.J.K. acknowledges the support from the Institute for Basic Science (IBS-R014-A2). K.W. and T.T. acknowledge support from the Elemental Strategy Initiative conducted by the MEXT, Japan and the CREST (JPMJCR15F3), JST. C.-Z. C. and K.T.L. acknowledge the support of The Croucher Foundation and HKRGC through C6026-16W, 16324216, 16307117 and 16309718.

Author contributions

K.C.F., M.N.A., K.T.L., and G.-H.L. conceived and supervised the project. Y.-B.C. fabricated the samples. Y.-B.C., J.-H.P. and H.-J.L. performed transport experiments. J.Y. and M.N.A. provided the WTe₂ crystal, and T.T. and K.W. provided the hexagonal boron nitride crystal. S.-B.S., B.J.K., and J.-H.K. collected and analysed polarized Raman spectrum. Y.X., C.-Z.C. and K.T.L. performed and analysed theoretical calculations for band spectrums and Fraunhofer patterns. Y.-B.C., Y.X., K.C.F., M.N.A., K.T.L., and G.-H.L. wrote the paper with inputs from C.-Z.C., J.-H.P., S.-B.S., and J.-H.K.

References

- 1 Armitage, N. P., Mele, E. J. & Vishwanath, A. Weyl and Dirac semimetals in three-dimensional solids. *Rev. Mod. Phys.* **90**, 015001 (2018).
- 2 Soluyanov, A. A. *et al.* Type-II Weyl semimetals. *Nature* **527**, 495-498 (2015).
- 3 Grushin, A. G. Consequences of a condensed matter realization of Lorentz-violating QED in Weyl semi-metals. *Phys. Rev. D* **86**, 045001 (2012).
- 4 Zyuzin, A. A. & Tiwari, R. P. Intrinsic anomalous Hall effect in type-II Weyl semimetals. *JETP Lett.* **103**, 717-722 (2016).
- 5 Ma, Q. *et al.* Observation of the nonlinear Hall effect under time-reversal-symmetric conditions. *Nature* **565**, 337-342 (2019).
- 6 Kang, K., Li, T., Sohn, E., Shan, J. & Mak, K. F. Nonlinear anomalous Hall effect in few-layer WTe₂. *Nat. Mater.* **18**, 324-328 (2019).
- 7 O'Brien, T. E., Diez, M. & Beenakker, C. W. J. Magnetic Breakdown and Klein Tunneling in a Type-II Weyl Semimetal. *Phys. Rev. Lett.* **116**, 236401 (2016).
- 8 Yu, Z.-M., Yao, Y. & Yang, S. A. Predicted Unusual Magnetoresponse in Type-II Weyl Semimetals. *Phys. Rev. Lett.* **117**, 077202 (2016).
- 9 Chen, C.-Z. *et al.* Asymmetric Josephson effect in inversion symmetry breaking topological materials. *Phys. Rev. B* **98**, 075430 (2018).
- 10 Pan, X.-C. *et al.* Pressure-driven dome-shaped superconductivity and electronic structural evolution in tungsten ditelluride. *Nat. Commun.* **6**, 7805 (2015).
- 11 Qi, Y. *et al.* Superconductivity in Weyl semimetal candidate MoTe₂. *Nat. Commun.* **7**, 11038 (2016).
- 12 Deng, K. *et al.* Experimental observation of topological Fermi arcs in type-II Weyl semimetal MoTe₂. *Nat. Phys.* **12**, 1105 (2016).
- 13 Sun, Y., Wu, S.-C., Ali, M. N., Felser, C. & Yan, B. Prediction of Weyl semimetal in orthorhombic MoTe₂. *Phys. Rev. B* **92**, 161107 (2015).
- 14 Qian, X., Liu, J., Fu, L. & Li, J. Quantum spin Hall effect in two-dimensional transition metal dichalcogenides. *Science* **346**, 1344-1347 (2014).
- 15 Fei, Z. *et al.* Edge conduction in monolayer WTe₂. *Nat. Phys.* **13**, 677-682 (2017).

- 16 Wu, S. *et al.* Observation of the quantum spin Hall effect up to 100 kelvin in a monolayer crystal. *Science* **359**, 76 (2018).
- 17 Tang, S. *et al.* Quantum spin Hall state in monolayer 1T'-WTe₂. *Nat. Phys.* **13**, 683-687 (2017).
- 18 Peng, L. *et al.* Observation of topological states residing at step edges of WTe₂. *Nat. Commun.* **8**, 659 (2017).
- 19 Cucchi, I. *et al.* Microfocus Laser–Angle-Resolved Photoemission on Encapsulated Mono-, Bi-, and Few-Layer 1T'-WTe₂. *Nano Lett.* **19**, 554-560 (2019).
- 20 Wang, Z., Wieder, B. J., Li, J., Yan, B. & Bernevig, B. A. Higher-Order Topology, Monopole Nodal Lines, and the Origin of Large Fermi Arcs in Transition Metal Dichalcogenides XTe₂ (X=Mo,W). Preprint at <https://arxiv.org/abs/1806.11116> (2018).
- 21 Bruno, F. Y. *et al.* Observation of large topologically trivial Fermi arcs in the candidate type-II Weyl semimetal WTe₂. *Phys. Rev. B* **94** (2016).
- 22 Zhang, W. *et al.* Quasiparticle interference of surface states in the type-II Weyl semimetal WTe₂. *Phys. Rev. B* **96**, 165125 (2017).
- 23 Ali, M. N. *et al.* Large, non-saturating magnetoresistance in WTe₂. *Nature* **514**, 205-208 (2014).
- 24 Ali, M. N. *et al.* Correlation of crystal quality and extreme magnetoresistance of WTe₂. *EPL* **110**, 67002 (2015).
- 25 Zhu, Z. *et al.* Quantum Oscillations, Thermoelectric Coefficients, and the Fermi Surface of Semimetallic WTe₂. *Phys. Rev. Lett.* **114**, 176601 (2015).
- 26 Li, P. *et al.* Evidence for topological type-II Weyl semimetal WTe₂. *Nat. Commun.* **8**, 2150 (2017).
- 27 Lee, C.-H. *et al.* Tungsten Ditelluride: a layered semimetal. *Sci. Rep.* **5**, 10013 (2015).
- 28 Song, Q. *et al.* The In-Plane Anisotropy of WTe₂ Investigated by Angle-Dependent and Polarized Raman Spectroscopy. *Sci. Rep.* **6**, 29254 (2016).
- 29 Courtois, H., Meschke, M., Peltonen, J. T. & Pekola, J. P. Origin of Hysteresis in a Proximity Josephson Junction. *Phys. Rev. Lett.* **101**, 067002 (2008).
- 30 Hart, S. *et al.* Induced superconductivity in the quantum spin Hall edge. *Nat. Phys.* **10**, 638-643 (2014).
- 31 Pribiag, V. S. *et al.* Edge-mode superconductivity in a two-dimensional topolog

- ical insulator. *Nat. Nanotechnol.* **10**, 593-597 (2015).
- 32 Lee, J. H. *et al.* Local and Nonlocal Fraunhofer-like Pattern from an Edge-Stepped Topological Surface Josephson Current Distribution. *Nano Lett.* **14**, 5029-5034 (2014).
- 33 Schindler, F. *et al.* Higher-order topology in bismuth. *Nat. Phys.* **14**, 918-924 (2018).
- 34 Ezawa, M. Second-order topological insulators and loop-nodal semimetals in Transition Metal Dichalcogenides XTe_2 ($X=Mo, W$). *Sci. Rep.* **9**, 5286 (2019).
- 35 Gray, M. J. *et al.* Evidence for Helical Hinge Zero Modes in an Fe-Based Superconductor. *Nano Lett.* **19**, 4890-4896 (2019).
- 36 Bovenzi, N. *et al.* Chirality blockade of Andreev reflection in a magnetic Weyl semimetal. *Phys. Rev. B* **96**, 035437 (2017).
- 37 Khanna, U., Kundu, A., Pradhan, S. & Rao, S. Proximity-induced superconductivity in Weyl semimetals. *Phys. Rev. B* **90**, 195430 (2014).
- 38 Faraei, Z. & Jafari, S. A. Induced superconductivity in Fermi arcs. *Phys. Rev. B* **100**, 035447 (2019).
- 39 Tang, F., Po, H. C., Vishwanath, A. & Wan, X. Efficient topological materials discovery using symmetry indicators. *Nat. Phys.* **15**, 470-476 (2019).
- 40 Wu, Y. *et al.* Observation of Fermi arcs in the type-II Weyl semimetal candidate WTe_2 . *Phys. Rev. B* **94**, 121113 (2016).

**Supplementary Information of
Evidence of Higher Order Topology in Multilayer WTe₂ from Josephson
Coupling through Anisotropic Hinge States**

Yong-Bin Choi¹, Yingming Xie², Chui-Zhen Chen^{2,†}, Jin-Ho Park¹, Su-Beom Song³, Jiho Yoon⁴, Bum Joon Kim^{1,5}, Takashi Taniguchi⁶, Kenji Watanabe⁶, Hu-Jong Lee¹, Jong-Hwan Kim³, Kin Chung Fong^{7,*}, Mazhar N. Ali^{4,*}, Kam Tuen Law^{2,*} and Gil-Ho Lee^{1,*}

¹Department of Physics, Pohang University of Science and Technology, Pohang, Republic of Korea

²Department of Physics, Hong Kong University of Science and Technology, Clear Water Bay, Hong Kong, China

³Department of Materials Science and Engineering, Pohang University of Science and Technology, Pohang, Republic of Korea

⁴Max Plank Institute for Microstructure Physics, Halle (Saale), Germany

⁵Center for Artificial Low Dimensional Electronic Systems, Institute for Basic Science (IBS), Pohang, Republic of Korea

⁶Research Center for Functional Materials, National Institute for Materials Science, Tsukuba, Ibaraki, Japan;

⁷Raytheon BBN Technologies, Quantum Information Processing Group, Cambridge, MA, USA

†Current address: Institute for Advanced Study and School of Physical Science and Technology, Soochow University, Suzhou 215006, China

*Correspondence and requests for materials should be addressed to K.C.F (kc.fong@raytheon.com), M.N.A. (maz@berkeley.edu), K.T.L. (phlaw@ust.hk), or G.-H.L. (lghman@postech.ac.kr).

S1. Magneto-transport on bulk and thin-flake WTe₂

Figure S1a show the magnetoresistance measurement of bulk WTe₂ crystal. WTe₂ was observed large magnetoresistance (MR)¹, here we also observe large MR up to 10,000 % at the perpendicular magnetic field, MR is defined as $(R_{xx}(B) - R_0)/R_0$, $R_0 = R_{xx}(B = 0)$. Nonlinear Hall resistance $R_{xy}(B)$ was observed because both electron and hole carrier type contribute Hall transport. Using classical two-band model for resistance, we assumed two carrier density and mobility^{2,3}.

$$R_{xy} = \frac{B[(n_h \mu_h^2 - n_e \mu_e^2) + (n_h - n_e) \mu_h \mu_e B^2]}{e[(n_h \mu_h + n_e \mu_e)^2 + (n_h - n_e) \mu_h^2 \mu_e^2 B^2]}$$

Electron carrier density and hole carrier density similar, but electron carrier density slightly larger than hole carrier density ($n_e = 4.08 \times 10^{25} \text{ m}^{-3}$, $n_h = 3.89 \times 10^{25} \text{ m}^{-3}$). From the classical two band model, electron and hole carrier mobility was calculated by $\mu_e = 2000 \times 10^{-4} \text{ m}^2/\text{V} \cdot \text{s}$, $\mu_h = 2040 \times 10^{-4} \text{ m}^2/\text{V} \cdot \text{s}$, respectively.

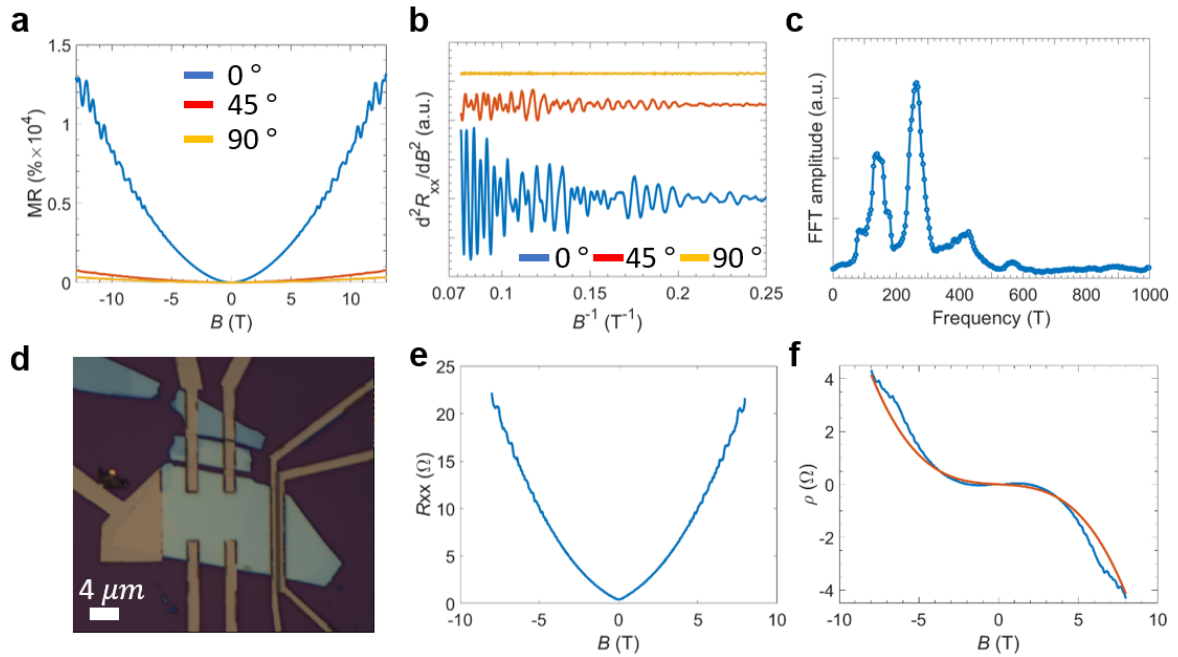


Figure S1 | Magneto transport measurements on bulk and thin-film WTe₂. **a**, Magnetoresistance (MR) with magnetic field perpendicular (blue), in-plane (yellow), and 45° (red) to the *ab* crystal plane. **b**, SdH oscillation as a function of inverse magnetic field perpendicular (blue), in-plane (yellow), and 45° (red) to the *ab* crystal plane. **c**, Fast Fourier transform of oscillatory magnetoresistance at 0°. **d**, Optical micrograph of Hall geometric

WTe₂ device. **e**, Measured R_{xx} of Hall geometric device at 290 mK. **f**, Measured R_{xy} (blue) of Hall geometric device with classical two band model fitting (red).

S2. Crystal axis identification from polarization-resolved Raman spectrum

Polarization-resolved Raman spectroscopy is utilized as an accurate and non-invasive characterization tool to determine the anisotropic crystal orientation. The polarizations of incident and scattered light are set in the parallel configuration while the crystal orientation of WTe₂ flakes relative the polarization is rotated by a half waveplate as described in methods section of the main text. The crystal axis can be determined from polarization-angle dependence of the Raman intensity following the previous works^{6,21,22}. Figure S2a, d, and g (Figure S3. a, and b) shows micrograph of a WTe₂ flake of Dev. A1, Dev. A2, and Dev. A3 (Dev. B1, and Dev. B2), respectively. The polarization direction (θ , red arrow) is varied from 0 to 360 degree with respect to the vertical direction (black solid line) of the micrograph. The Colour-coded plot of Raman intensity are shown in Fig. S2. b, e, and h (Figure S3. c, and d). The Raman signals originate from the A₁ modes of Td-WTe₂ crystals which all show polarization-angle dependence. For example, the Raman modes around at 165 cm⁻¹ and 213 cm⁻¹ show characteristic two-fold patterns (Figure S2.c, f, and i), (Figure S3. e, and f) in their polarization angle dependence. Intensity maximum of ~ 165 cm⁻¹ and 213 cm⁻¹ Raman modes appear when the polarization aligns respectively with the *a*-axis and *b*-axis, which is previously established based on high-resolution atomic force microscopy and Raman tensor analysis^{6,21,22}.

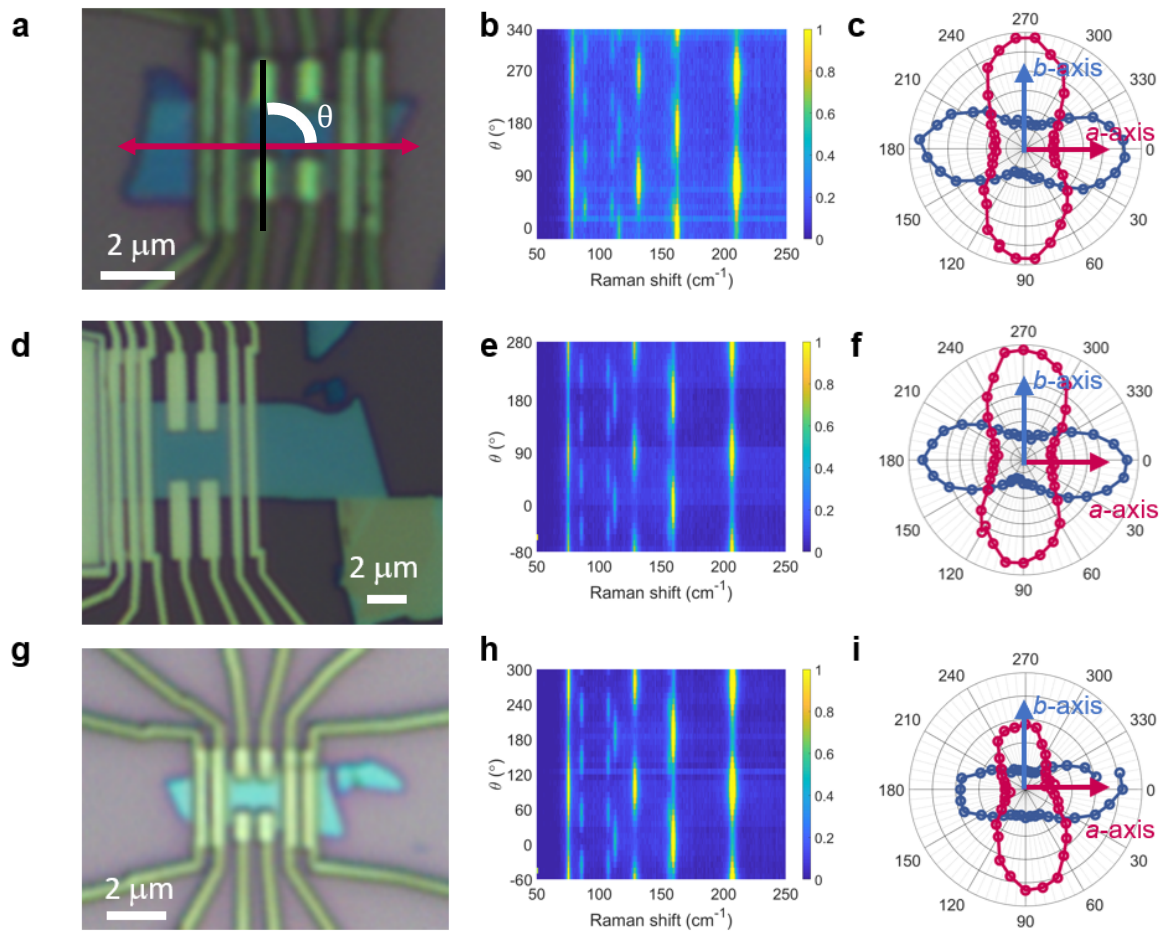


Figure S2 | Polarized Raman spectroscopy for determining crystal axis for Dev. A1, A2, and A3. **a, d, g** Optical micrograph of WTe₂ devices for Dev. A1 (**a**), Dev. A2 (**d**), and Dev. A3 (**g**), respectively. **b, e, h**, Colour-coded plot of Raman intensity as a function of relative crystal angle and relative Raman shift for Dev. A1 (**b**), Dev. A2 (**e**), and Dev. A3 (**h**), respectively. **c, f, i** Polar plots of Raman intensity with a function of the polarization angle. Raman modes at ~ 165 (blue circles and line) and 213 cm^{-1} (red circles and line) show characteristic two-fold patterns where intensity maximums align to *a*-axis and *b*-axis of WTe₂ crystals for Dev. A1 (**c**), Dev. A2 (**f**), and Dev. A3 (**i**), respectively.

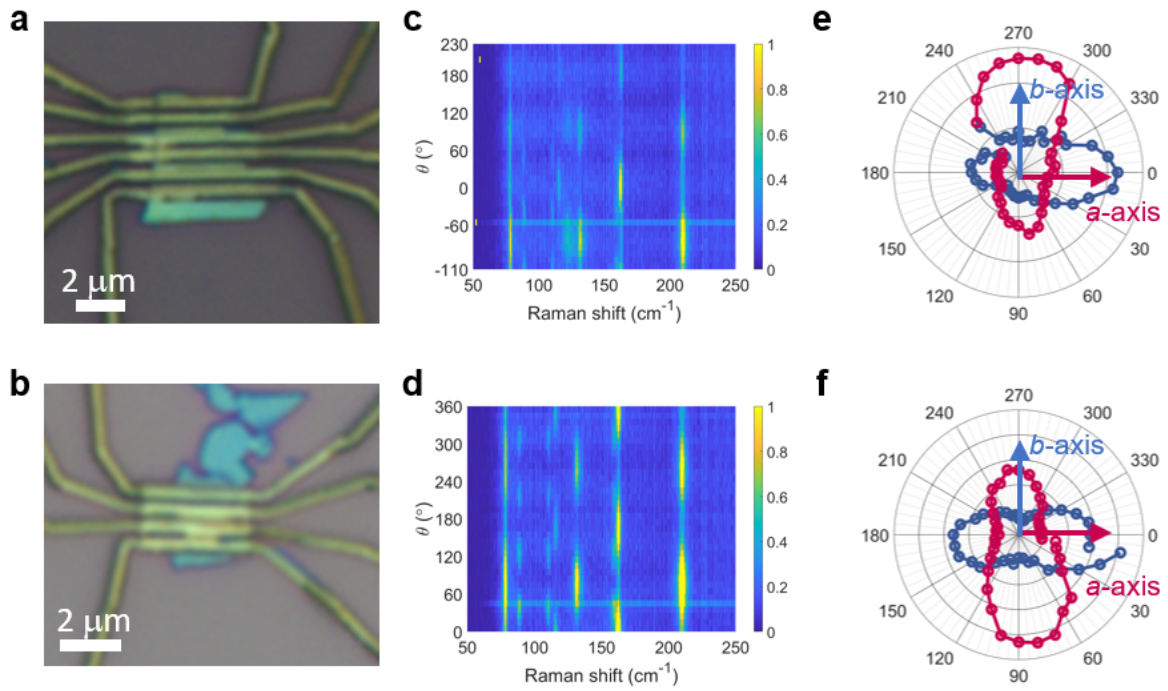


Figure S3 | Polarized Raman spectroscopy for determining crystal axis for Dev. B1 and B2. **a, b** Optical micrograph of WTe₂ devices for Dev. B1 (**a**), and Dev. B2 (**b**), respectively. **c, d**, Colour-coded plot of Raman intensity as a function of relative crystal angle and relative Raman shift for Dev. B1 (**c**), and Dev. B2 (**d**), respectively. **e, f**, Polar plots of Raman intensity with a function of the polarization angle. Raman modes at ~ 165 (blue circles and line) and 213 cm^{-1} (red circles and line) show characteristic two-fold patterns where intensity maximums align to *a*-axis and *b*-axis of WTe₂ crystals for Dev. B1 (**e**), and Dev. B2 (**f**), respectively.

S3. Summary of WTe₂ Josephson junction series of Dev. A, and Dev. B

We fabricated more WTe₂ Josephson junction device along *a*-axis and *b*-axis of the WTe₂ crystal of Dev. A1 to Dev. A4 and Dev. B1 to Dev. B4 and summarized in Table S1. Here, Dev. A1 and Dev. B1 represent Dev. A and Dev. B in the main text, respectively. We also observed non-vanishing interference pattern for series of Dev. A (Fig. S7) and conventional single slit interference pattern for series of Dev. B (Fig. S8)

	Name	I_c (μA)	R_N (Ω)	$I_c R_N$ (μV)	Length (nm)	Width (μm)	Thickness (nm)	$R_N \times W \times T/L$ ($\mu \Omega \cdot m$)
Device along a-axis	Dev. A1	0.7	32	22.4	190	2.31	13.2	5.14
	Dev. A2	0.9	7	6.3	230	5.18	22	3.47
	Dev. A3	1.7	20	34	91	2.23	14	6.86
	Dev. A4	2.5	3.5	8.8	110	4.30	27.2	3.72
Device along b-axis	Dev. B1	0.5	6	3.0	100	3.33	25	5.00
	Dev. B2	0.1	25	2.5	120	2.35	16.7	8.18
	Dev. B3	0.08	30	2.4	130	1.82	14.6	6.13
	Dev. B4	0.1	15	1.5	150	3.78	18.8	7.11

Table S1 | Summary of devices

S4. Inverse Fourier transform technique

Josephson junction with a perpendicular magnetic field, the magnitude of the maximum critical current $I_c^{max}(B)$ is an absolute value of Josephson current $I_J(\phi)$ and the critical current of the junction modulated with external magnetic field and the modulation depending on Josephson current density in real space. For example, when uniform Josephson current density flow through the junction, the maximum critical current show single-slit Fraunhofer interference pattern. However, when Josephson current density flow only to the edge, the interference pattern shows SQUID interference pattern. In our experiment, we can assume non-vanishing Interference pattern caused by uniform and edge enhanced Josephson current density.

The total Josephson current through junction (I_J) and critical current are following the equations,

$$I_J(\phi) = \int_{-L/2}^{L/2} dx J(x) e^{i\phi(x)}, \quad \text{Eq. (1)}$$

$$I_c^{max} = |I_J(\phi)|,$$

Here, $J(x)$ is Josephson current distribution in real space, $\phi(x) = \phi_0 + 2\pi B L d_{\text{eff}} x / \Phi_0$, initial phase different ϕ_0 , effective distance d_{eff} , and magnetic flux quantum $\Phi_0 = h/2e$.

The equation of $I_J(\phi)$ is a Fourier transform of a Josephson current distribution in real space $J(x)$. Therefore, we can reconstruct Josephson current density in real space using inverse Fourier transform of Josephson current (I_J).

First, from the experimentally acquired interference pattern, extract critical current $I_C^{\text{max}}(B)$. For an ideal situation, Josephson current has only even current term, because odd part of Eq. (1) vanish from the integration. Thus, equation (1) becomes Fourier transform of even current density $I_J^{\text{E}}(\phi) = \int_{-L/2}^{L/2} dx J_E(x) \cos(\phi(x))$. Now then, from the critical current $I_C^{\text{max}} = |I_J(\phi)|$, we can recover the even Josephson current $I_J^{\text{E}}(\phi)$ by flipping the sign of every other lobe of the extracted I_C^{max} .

However, our situation is not an ideal such as non-zero resistance between two lobes. Thus, the odd part of Josephson current cannot be ignored, so total Josephson current should be considered not only even part but also odd part of Josephson current.

$$I_J(\phi) = I_E(\phi) + iI_O(\phi) = \int_{-L/2}^{L/2} dx [J_E(x) \cos(\phi(x)) + i J_O(x) \sin(\phi(x))],$$

Therefore, considering the odd part of Josephson current, the observed critical current become $I_C^{\text{max}} = |I_J(\phi)| = \sqrt{I_E^2(\phi) + I_O^2(\phi)}$. This equation means that when even Josephson current $I_E(\phi)$ is minimal, the odd Josephson current $I_O(\phi)$ is dominant. From this, $I_O(\phi)$ can be recovered (Fig. S4). By performing inverse Fourier transform, we can reconstruct Josephson current distribution in real space as⁴

$$J(x) = \left| \frac{1}{2\pi} \int_{-a/2}^{a/2} d\phi I_J(\phi) e^{-i\alpha x} \right|, \text{ with } \alpha = 2\pi B d_{\text{eff}} L / \Phi_0.$$

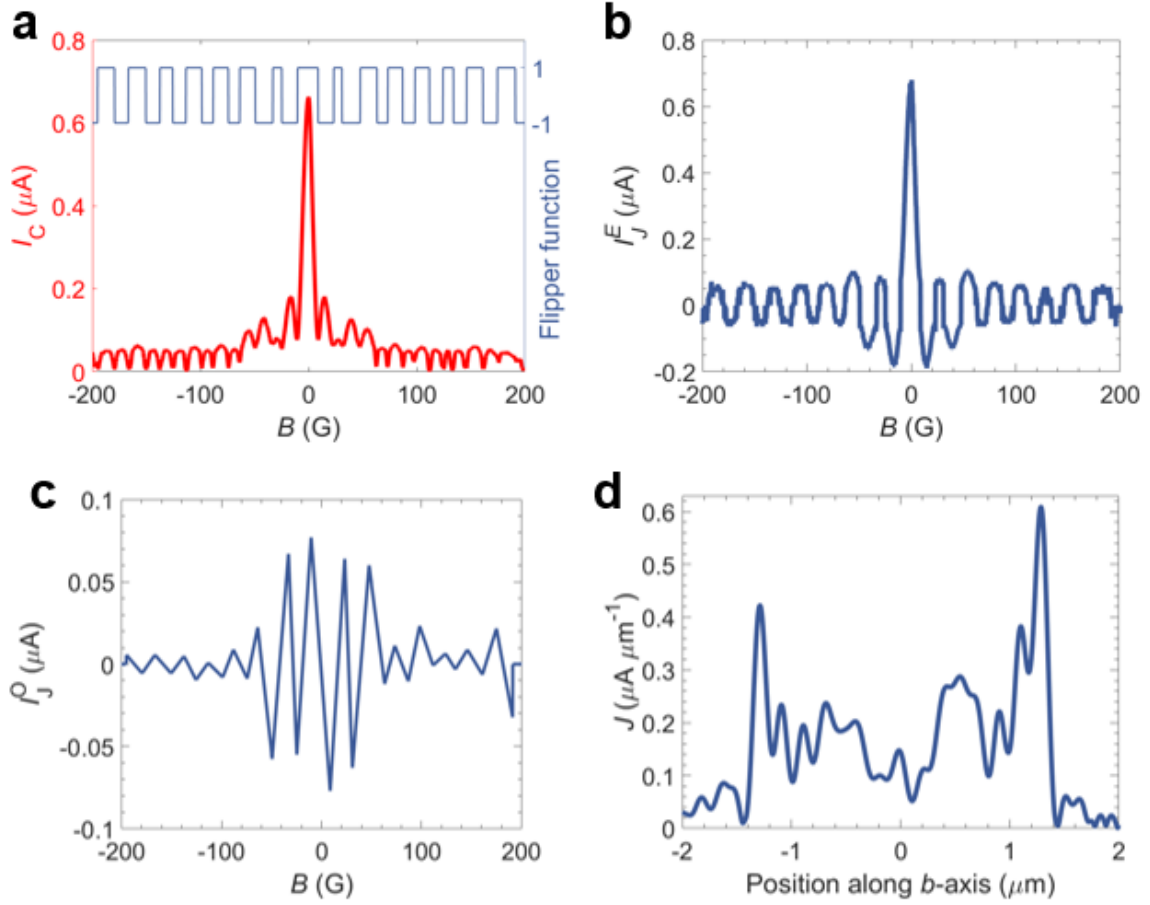


Figure S4 | Inverse Fourier Transform of critical current. **a**, (red)extracted critical current from observed Fraunhofer interference pattern and (blue)flipper function. **b**, The recovered even part of Josephson current $I_J^E(\phi)$. **c**, The recovered odd part of Josephson current $I_J^O(\phi)$. **d**, The reconstructed Josephson current density in real space along b -axis.

S5. Bulk-Boundary correspondence

The wave-function of the hinge states given by $H(\mathbf{k})$ are shown in Fig. S5. It can be found that the hinge states mainly locate at the opposite hinges of the 3D system along a -axis. There are some finite values of wave-function coming from the surfaces perpendicular to a -axis. In contrast, the surfaces parallel to a -axis are well gapped. This bulk-boundary correspondence can be understood from the two fold symmetry in $H(k)$, parity symmetry $P = \tau^z$ and mirror symmetry $M_a = i\sigma^y$, where $P\mathbf{k} \rightarrow -\mathbf{k}$, $M_a\mathbf{k} \rightarrow (-k_a, k_b, k_c)$. The location of the hinge states can be simply determined by the sign of mass m_r at different surfaces⁵, which is defined within the low energy surface Hamiltonian and gaps the Dirac surface states.

In the inversion symmetric higher order topological insulators (HOTIs), the mass changes sign under inversion: $m_{-r} \rightarrow -m_{-r}$. And according to the surface Dirac theory⁵, the surface parallel to the mirror plane remains gapless in this scenario. The hinge states exist at where the two adjacent surface forms domain wall, namely the sign of mass changes. Thus, the localization feature of wave-function in Fig. S5 is consistent with boundary correspondence of the HOTI phase in presence of both inversion and mirror symmetry. More examples and detail analysis about the constraint of inversion and mirror symmetry in HOTI can be found in Ref.^{5,6}. However, the inversion symmetry is broken for Td-WTe₂. In Ref.⁷, they proposed Td-WTe₂ are very likely to be inversion-broken HOTI phase. In this case, there is no obvious constraint to forbid the mass terms even for the surface parallel to the mirror plane. However, we still attempt to believe that the hinge states are more localized for the hinges perpendicular to the mirror plane, considering the non-inversion symmetric HOTI in Td-WTe₂ is inherited from inversion symmetric HOTI in 1T'-WTe₂⁷.

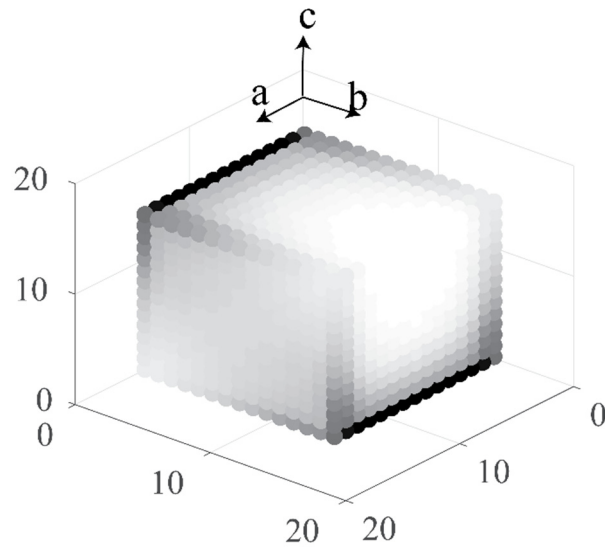


Figure S5 | Localized hinge modes of the minimal model of a HOTI with the same topology and symmetries as WTe₂ with open boundary conditions in all directions.

S6. Graphite Josephson junction

We fabricate graphite-based Josephson junction as a control experiment of WTe₂ Josephson junction because graphite has isotropic band structure while WTe₂ has not and

graphite-based Josephson junction has expected isotropic transport. The fabrication process completely same as a fabrication process of WTe₂ Josephson junction as described in main text. To reduce conduction of graphite, we choose thinner flake than WTe₂ flake (10~20 nm).

Here, we investigate two Josephson junctions in the one graphite device, GJJ-JJ1 of $(L, W, t) = (250 \text{ nm}, 7.1 \text{ } \mu\text{m}, 5.8 \text{ nm})$ and GJJ-JJ2 of $(L, W, t) = (200 \text{ nm}, 7.1 \text{ } \mu\text{m}, 5.8 \text{ nm})$ in Fig. S6a. The interference patterns were measured at 0.1 K (Figs. S6b and d). The critical current at field center is 3.5 μA for GJJ-JJ1 and 3.3 μA for GJJ-JJ2. The $I_c R_N$ products are 35 μV and 31 μV for GJJ-JJ1 and GJJ-JJ2, respectively, which are in the same order of magnitude of those of Dev. A and Dev. B. The oscillation period of $\Delta B = 4.5 \text{ G}$ (5.3 G) of GJJ-JJ1 (GJJ-JJ2) gives $L' \sim 200$ (175) nm, which corresponds to the nearly half width of Nb electrodes. Reconstruction of uniform spatial distribution of Josephson current density (Figs. S6c, and e) inferred observed unconventional interference pattern of WTe₂ devices are not artefacts introduced during fabrication process.

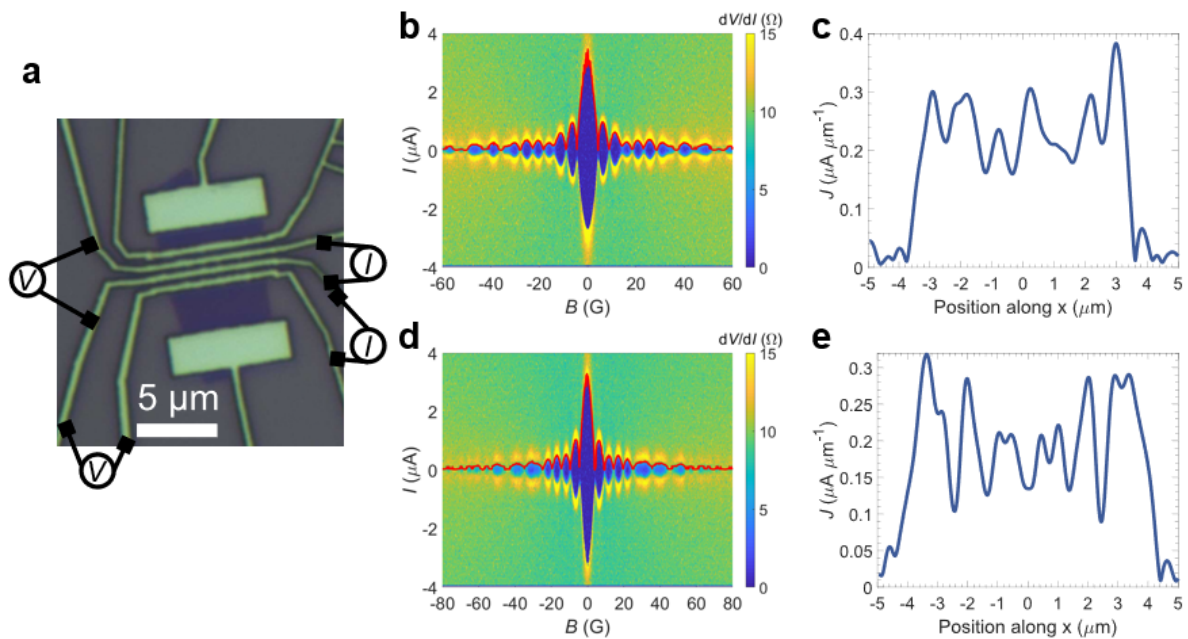


Figure S6 | Control experiment device Graphite Josephson junction. **a**, Optical micrograph of Graphite Josephson junction. **b**, **d**, Colour-coded plot of differential resistance dV/dI as a function of bias current I and perpendicular external magnetic field B for JJ1 (**b**) and JJ2 (**d**). Red solid lines represent extracted Josephson critical current. **c**, **e**, Extracted spatial distribution of Josephson current density J for GJJ-JJ1 (**c**) and GJJ-JJ2 (**e**).

S7. Other WTe₂ Josephson junction devices along *a*-axis

Figure S7 show other Nb-WTe₂-Nb Josephson junction device of Dev. A2 (Figs. 7a, b, and c), Dev. A3 (Figs. S7d, e, and f), and Dev. A4 (Figs. S7g, h, and i). The fabrication process completely same as a described in main text. Here, Dev. A2, Dev. A3, and Dev. A4 was measured under 20 mK. Information of devices are summarized in Table S1. For Dev. A3 and Dev. A4 superconducting contact is Nb as same as Dev. A1 and series of Dev. B. Whereas, Dev. A2 used superconducting contact for Aluminum (Al). Therefore, the side lobes decayed over 70 G because of the small critical magnetic field (~ 100 G) of Al (Fig. S7b). The oscillation period of $\Delta B=7.0$ G gives $L'\sim 195$ nm, which corresponds to the nearly half width of Al electrodes. Josephson current density in real space was reconstructed by using inverse Fourier transform and confirmed edge-enhanced transport. Gaussian fitting for each left(right) edge enhancement with width around 234(334) nm for Dev. A2. We observed SQUID-like interference pattern, the lobes dose not decay until 100 G for a Dev. A3. The oscillation period of $\Delta B=14.7$ G, and 8.85 G gives $L'\sim 170$ nm, and 210 nm, which corresponds to the nearly half width of Nb electrodes for Dev A3 for Dev. A4, respectively. Using inverse Fourier transform, we check edge-enhanced transport and Gaussian fitting for each left(right) edge enhancement with width around 144(271) nm, and 372(575) nm for Dev A3, Dev A4, respectively. By considering a short ballistic junction limit ($eI_{J,h,Nb(Al)}R_{N,h} = \pi\Delta_{Nb(Al)}$) the maximum theoretical value of $I_{J,h,Nb(Al)} = 140(22)$ nA for a single hinge state, where $R_{N,h} = h/e^2$ is the normal resistance for a single hinge state and $\Delta_{Nb(Al)} = 1.763k_B T_{c,Nb(Al)}$ is the BCS superconducting gap of the Nb(Al) electrode with $T_{c,Nb(Al)} = 7.5(1.2)$ K. $I_{J,side}$ of Dev. A2, Dev. A3 and Dev. A4 is 8.8, 11 and 33 nA for left edge and 55, 65 and 143 nA for right edge, respectively, as visible as the shaded areas in Figs. S7c,f, and i. These values are comparable to or less than the maximum theoretical value $I_{J,h,Nb(Al)}$.

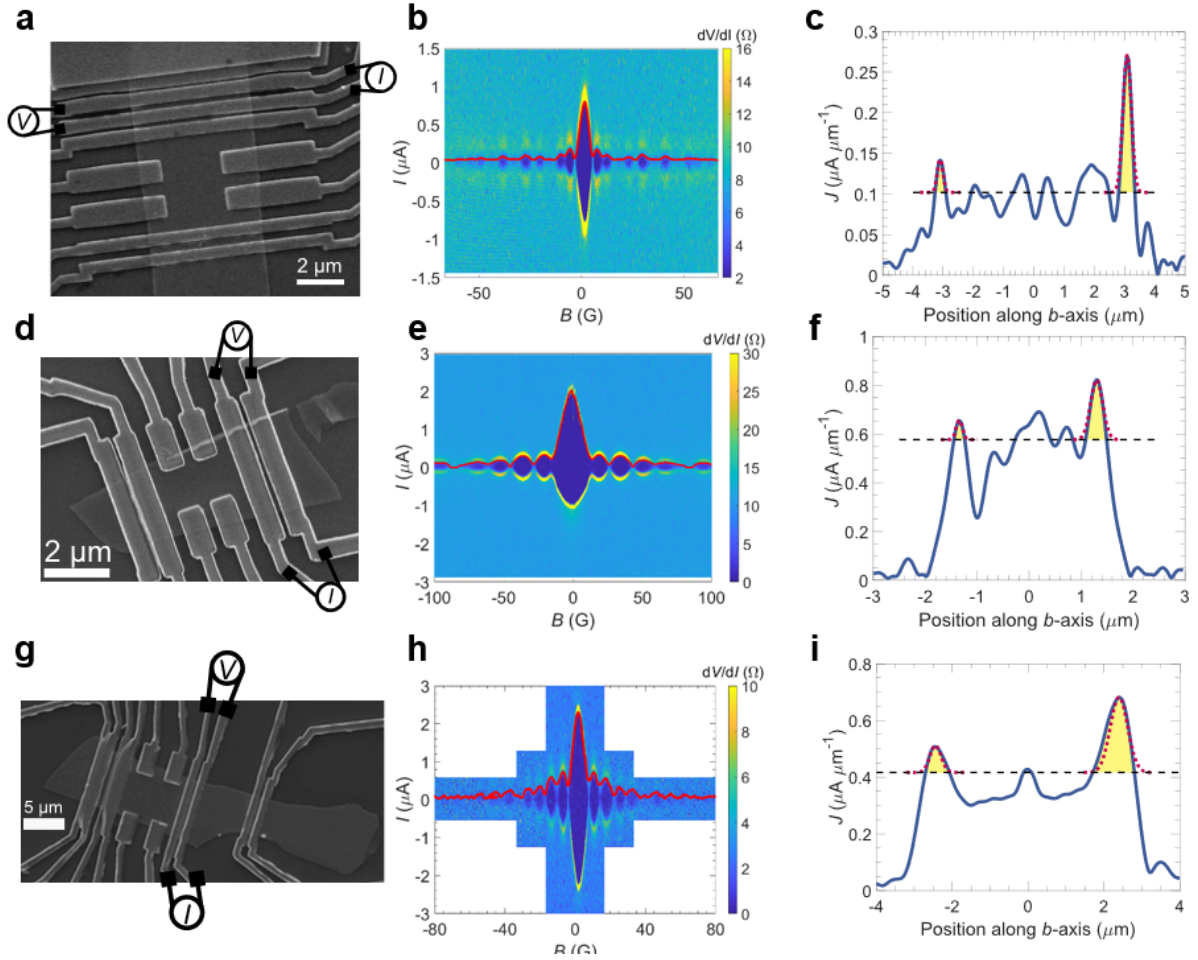


Figure S7 | Other devices of Dev. A2, A3 and A4. **a, d, g**, Scanning electron micrograph of Dev. A2, A3 and A4 with measurement configuration, respectively. **b, e, h**, Colour-coded plot of differential resistance dV/dI as a function of bias current I and perpendicular external magnetic field B for Dev. A2 (**b**), Dev. A3 (**e**) and Dev. A4 (**h**). Red solid lines represent extracted Josephson critical current. **c, f, i**, Extracted spatial distribution of Josephson current density J for Dev. A2 (**c**), Dev. A3 (**f**) and Dev. A4 (**i**). Dotted line represents Gaussian fitting for each edge enhancement.

S8. Other WTe₂ Josephson junction devices along b -axis

Figure S8 show other Nb-WTe₂-Nb Josephson junction device of Dev. B2 (Figs. S8a and b), Dev. B3 (Figs. S8c and d), and Dev. B4 (Figs. S8e and f). Here, Dev. B2, Dev. B3, and Dev. B4 was measured under 30 mK. Information of devices are summarized in Table S1. Because of anisotropic transport, we cannot observe non-vanishing or ordinary interference

pattern and critical current much smaller than Dev. A.

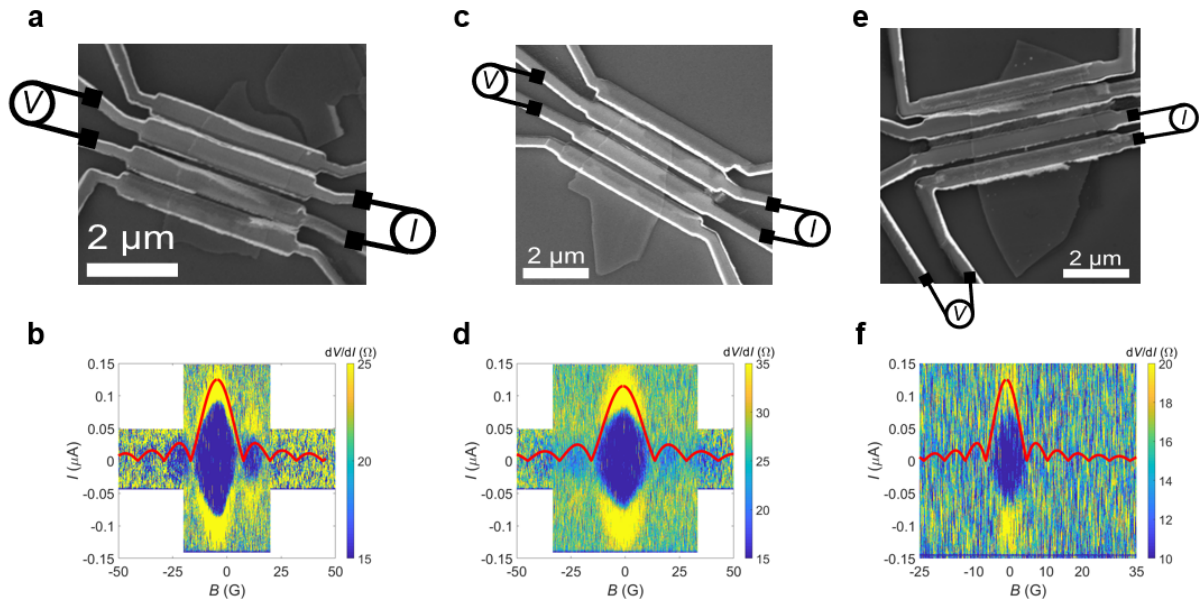


Figure S8 | Other devices of Dev. B2, B3 and B4. a, c, e, Scanning electron micrograph of Dev. B2, B3 and B4 with measurement configuration, respectively. **b, d, f,** Colour-coded plot of differential resistance dV/dI as a function of bias current I and perpendicular external magnetic field B for Dev. B2 (**b**), Dev. B3 (**d**) and Dev. B4 (**f**).

References

- 1 Ali, M. N. *et al.* Large, non-saturating magnetoresistance in WTe₂. *Nature* **514**, 205-208 (2014).
- 2 Woods, J. M. *et al.* Suppression of Magnetoresistance in Thin WTe₂ Flakes by Surface Oxidation. *ACS Appl. Mater. Interfaces* **9**, 23175-23180 (2017).
- 3 Zhu, Z. *et al.* Quantum Oscillations, Thermoelectric Coefficients, and the Fermi Surface of Semimetallic WTe₂. *Phys. Rev. Lett.* **114**, 176601 (2015).
- 4 Hart, S. *et al.* Induced superconductivity in the quantum spin Hall edge. *Nat. Phys.* **10**, 638-643 (2014).
- 5 Khalaf, E., Po, H. C., Vishwanath, A. & Watanabe, H. Symmetry Indicators and Anomalous Surface States of Topological Crystalline Insulators. *Phys. Rev. X* **8**, 031070 (2018).

- 6 Geier, M., Trifunovic, L., Hoskam, M. & Brouwer, P. W. Second-order topological insulators and superconductors with an order-two crystalline symmetry. *Phys. Rev. B* **97**, 205135 (2018).
- 7 Wang, Z., Wieder, B. J., Li, J., Yan, B. & Bernevig, B. A. Higher-Order Topology, Monopole Nodal Lines, and the Origin of Large Fermi Arcs in Transition Metal Dichalcogenides XTe_2 ($X=Mo,W$). Preprint at <https://arxiv.org/abs/1806.11116> (2018).